Journal of Applied Fluid Mechanics, Vol. 12, No. 5, pp. 1599-1614, 2019.
Available online at www.jafmonline.net, ISSN 1735-3572, EISSN 1735-3645.
DOI: 10.29252/jafm.12.05.29839

Large Eddy Simulation of Compressible Parallel Jet Flow and Comparison of Four Subgrid-Scale Models

Q. Liu[1], Y. H. Dong[2] and H. Lai[1 †]

[1] *School of Mechanical and Power Engineering, East China University of Science and Technology, Shanghai 200237, P. R. China*

[2] *Shanghai Institute of Applied Mathematics and Mechanics, Shanghai University, Shanghai 200072, P. R. China*

[†]*Corresponding Author Email:* hlai@ecust.edu.cn

(Received November 11, 2018; accepted January 20, 2019)

ABSTRACT

Large eddy simulations of a three-dimensional (3D) compressible parallel jet flow at Mach number of 0.9 and Reynolds number 2000 are carried out. Four subgrid-scale (SGS) models, namely, the standard Smagorinsky model (SM), the selective mixed scale model (SMSM), the coherent-structure Smagorinsky model (CSM) and the coherent-structure kinetic-energy model (CKM) are employed, respectively, and compared. The purpose of the study is to compare the SGS models and to find their suitability of predicting the flow transition in the potential core of the jet, and so as to provide a reference for selecting SGS models in simulating compressible jet flows, which is a kind of proto-type flow in fluid dynamics and aeroacoustics. A finite difference code with fourth-order spatial and very low storage third-order explicit Runge-Kutta temporal schemes is introduced and employed for calculation. The code, which was previously designed for simulating shock/boundary-layer interactions and had been widely validated in simulating a variety of compressible flows, is rewritten and changed into parallelized using the OpenMP protocol so that it can be run on memory-shared multi-core workstations. The computational domain size and the index of LES resolution quality are checked to validate the simulations. Detailed comparisons of the four SGS models are carried out. The results of averaged flow-field including the velocity profiles and the developments of shear-layer, the instantaneous vortical flows and the viscous dissipation, the predicted turbulence statistics and the balances of momentum equation are studied and compared. The results show that although the normalized developed velocity profiles are well predicted by the four SGS models, the length of the potential core and the development of the shear-layer reveal that the SM has excessive SGS viscosity and is therefore too dissipative to correctly predict the flow transition and shear-layer expansion. The model smears small vortical scales and lowers down the effective Reynolds number of the flow because of the over-predicted SGS viscosity and dissipation. The turbulence statistics and the balances of momentum equation have also confirmed the excessive dissipation of the SM. The CKM is also found to over-predict the SGS viscosity. Compared with these two models, the SMSM and the CSM have performed well in predicting both the averaged and the instantaneous flow-fields of the compressible jet. And they are localized models which are computationally efficient and easy for coding. Therefore, the SMSM and the CSM are recommended for the LES of the compressible Jet.

Keywords: Jet flow; LES; Localized SGS model; Selective mixed scale model; Coherent-structure Smagorinsky model; Coherent-structure kinetic-energy model.

1. INTRODUCTION

Compressible jet flows exhausted by engines are one of the main sources of noise in aircrafts, which has become a serious environmental problem (Sandham *et al.*, 2006). According to the aeroacoustics theory, which is pioneered by Lighthill (1952) and has achieved great success in the past more than 60 years, jet noises are highly relevant to the turbulent flow structures (Tam, 1998; Wan *et al.*, 2013). By so far, though it is well known that jet flows involve phenomena such as the potential core, shear layers, transition of turbulence, pairing of vortices, development and breakdown of large-scale vortices, the difficulties arise from the turbulence are still obstacles for understanding the mechanism of sound generation.

There are well-documented experimental results

about jet flows in which the characteristics of averaged flow field and large statistical structures have been revealed. These include the early experiments of Bradbury (1965) in which the establishment of the self-preservation in downstream of the nozzle exit is studied, and the measurement of correlations by Everitt *et al.* (1978) which unveiled the no-similarity of large-scale statistical structures as a kind of 'local flapping' in a moving stream. Modern flow visualization techniques such as the laser induced fluorescence (LIF) and particle image velocimetry (PIV) have also been applied to study the flow details in jets by Hui *et al*. (1999) and Tinney and Jordan (2008), respectively. The developments of the turbulent structures have been well described. However, due to the difficulties in the measurement of dissipation in highly turbulent flows, the nature of the small-scale turbulence is hard to accurately ascertain. As pointed by Uzun *et al*. (2012), although experiments provide useful information for understanding the jet flows, they are expensive and can supply a relatively limited flow detail. For example, the flow within the first or two diameters immediately downstream of the nozzle exit contains crucial information on jet shear layer initial conditions and has a profound effect on the complex flow phenomena in further downstream. However, even modern experimental methods have difficulty in measuring such flow because of the thin shear layers and the resultant steep velocity gradients in that region. Based on these backgrounds, high resolution numerical simulation becomes very attractive and necessary for revealing the flow detail in turbulent jet flows.

With the fast advances in computational techniques, successful numerical methods for turbulence simulation have been developed. These methods, categorized according to the flow detail resolved and the computational costs, are the direct numerical simulation (DNS), the large-eddy simulation (LES), and the Reynolds-average Navier-Stokes (RANS) methods. Although DNS, in principle, is capable of resolving all fluid dynamics and acoustics scales in jet flow, it has been limited by available computing resources to 2D and low-Reynolds-number cases (Stanley *et al*., 2002; Klein *et al*., 2003). The RANS methods for jet flows (Tam and Auriault, 1999), on the other hand, are generally applied to study the averaged flow-field and are often regarded as too crude for studying the mechanism of sound generation in the engineering context (Lai and Luo, 2007). In between of the DNS and the RANS methods, LES is a good balance for resolving the turbulence and the computational cost. Indeed, LES methods have been widely employed to study the jet flows in the past two decades. Excellent reviews on the LES investigations of jet flows have been provided by Bodony and Lele (2008) and Uzun and Hussaini (2012). Generally saying, for the purpose of resolving the flow detail, high-fidelity numerical algorithms and the sub-grid scale (SGS) models are the two key issues.

A review of all SGS models is far beyond the knowledge of the present authors and is not attempted here; readers may refer to the reviews in Vreman (1995) and Sagaut (2007) for some clues. Basically, the usage of SGS models is to account for the effects of sub-grid scale vortices on the resolved turbulent quantities (Piomelli, 1999). The early Smagorinsky model (SM) which has constant coefficient in the eddy-viscosity is known to be too dissipative and results in weak correlations between the modeled and the physical turbulent stresses. In order to overcome such defects, the dynamic Smagorinsky models (DSM) based on the Germano identity were introduced by researchers. By so far, DSM models are widely applied to study the jet flows (Hu *et al.*, 2003; Wan, *et al*., 2013). In the DSM models, Lilly's least square method is often employed to dynamically adjust the model coefficient. In such procedure, the flow field is theoretically required to have a homogeneous direction in which the filtered stresses can be averaged so as to find the local model coefficient. However, such requirement is not reasonable. Firstly, the three-dimensional flows occurred in engineering are basically impossible to have a homogeneous direction. Secondly, even for a flow in which may has a homogeneous direction, the average operation is only a strategy to prevent numerical instability; it lacks a rationale in physics. And thirdly, for large scale parallelized calculations, additional data exchanges between processors are unavoidable in the averaging operation, which is not computationally efficient. Seeing from these, localized SGS models are preferred, and easing the excessive dissipation of the SM is an expectation.

In this paper, three localized SGS models are considered and compared in calculation of a parallel jet flow at Mach 0.9. The problem is simple in flow configuration but rich in flow phenomena, while Mach 0.9 is an approximated flow condition for jet engines in subsonic civil aircrafts (Bodony and Lele, 2008). The SGS models are the selective mixed-scale model (SMSM) proposed by Lenormand *et al*. (2000), the coherent-structure Smagorinsky model (CSM) and the coherent-structure kinetic-energy model (CKM) both of which are proposed by Kobayshi (2005). For a sensible comparison, the SM is also included. In the SMSM, a selective function based on local angular fluctuation of the vorticity is introduced so as to predict the intermittent phenomena in transitional flows. The model has been validated in the simulation of the compressible wall bounded flows (Lenormand *et al*., 2000), the flow around airfoil at near stall condition (Mary and Sagaut, 2002), and in the cavity flows (Larchevêque *et al*., 2003). The CSM (Kobayshi, 2005) is based on the relationship between energy dissipation and coherent structures (Tanahashi, 1997), and its model coefficient is adjusted by a coherent structure function. The model has been tested in a series of incompressible turbulent flows including rotating and non-rotating channel flows, backward-facing step flows and staggered jets in crossflows; it is shown to have a similar accuracy to that obtained by the DSM (Kobayshi, 2005). The CKM is also based on a function of coherent structures, while the sub-grid scale kinetic energy is used as the velocity scale in

evaluating the turbulent viscosity. Together with the SM, all the four models are localized, so they have no need of any homogeneous direction or averaging in finding the model coefficients. The purpose of this comparison is to find the suitability of predicting the viscosity and flow transition in the potential core of the jet, and to provide a reference for selecting SGS models in simulating compressible jet flows.

The remaining contents of the present paper are arranged in four sections. Section 2 describes the governing equations for LES, the SGS models for comparison, the discretization and solution approach for the equations. Section 3 presents the preparations of simulating the jet. These include the setting up of the computational domain, the grids, boundary and initial conditions. And a check of the settings including the domain size and the grid sensitivity of the LES is provided. In section 4, the predicted results of both the averaged and the instantaneous jet flow fields are carefully studied, and the four SGS models are compared. Finally, conclusions of the comparison are summarized in Section 5.

2. NUMERICAL MODELS AND METHODOLOGY

2.1 Governing Equations

In large eddy simulation, the filtered compressible Navier-Stokes equations consist of the conservation laws of mass, momentum and energy. The governing equations can be written in a dimensionless form as follows (Vreman, 1995):

$$\frac{\partial \bar{\rho}}{\partial t}+\frac{\partial}{\partial x_j}\left(\bar{\rho}\tilde{u}_j\right)=0, \tag{1}$$

$$\frac{\partial}{\partial t}\left(\bar{\rho}\tilde{u}_i\right)+\frac{\partial}{\partial x_j}\left(\bar{\rho}\tilde{u}_i\tilde{u}_j\right)+\frac{\partial \bar{p}}{\partial x_i}-\frac{\partial \sigma_{ji}}{\partial x_j}=-\frac{\partial \bar{\rho}\tau_{ji}}{\partial x_j} \tag{2}$$

$$\begin{aligned}&\frac{\partial E_T}{\partial t}+\frac{\partial}{\partial x_j}\left[\left(E_T+\bar{p}\right)\tilde{u}_j\right]-\frac{\partial}{\partial x_j}\left(\sigma_{ji}\tilde{u}_i\right)+\frac{\partial q_j}{\partial x_j}\\&=-\tilde{u}_i\frac{\partial \bar{\rho}\tau_{ji}}{\partial x_j}-\frac{\partial q_j^{sgs}}{\partial x_j}\end{aligned} \tag{3}$$

where the summation convention for repeated indices is used. Top scripts '-' and '~' denote grid-filtered and mass-weighted (Favre) filtered variables, respectively. The filtered velocity vector is denoted by $\tilde{\boldsymbol{u}}$, with $\tilde{u}_i$ as its Cartesian components. $\bar{\rho}$ and $\bar{p}$ are the density and pressure, respectively. The total energy is calculated by

$$E_T=\frac{\bar{p}}{\gamma-1}+\frac{1}{2}\bar{\rho}\tilde{u}_i^2, \tag{4}$$

where γ is the ratio of specific heats. The filtered prefect gas law is

$$\bar{p}\gamma M^2=\bar{\rho}T, \tag{5}$$

where T is temperature while M is Mach number. The viscous stress

$$\sigma_{ij}=\left(\mu(T)/Re\right)S_{ij}\left(\tilde{\boldsymbol{u}}\right), \tag{6}$$

$$\text{where } S_{ij}\left(\tilde{\boldsymbol{u}}\right)=\frac{\partial \tilde{u}_i}{\partial x_j}+\frac{\partial \tilde{u}_j}{\partial x_i}-\frac{2}{3}\delta_{ij}\frac{\partial \tilde{u}_k}{\partial x_k} \tag{7}$$

is the strain rate, δ_{ij} is the Kronecker delta which has $\delta_{ij}=1$ if $i=j$ and $\delta_{ij}=0$ if $i\neq j$. μ is the viscosity and is calculated by the Sutherland law,

$$\mu(T)=T^{\Omega}\ (\Omega=0.76 \text{ for air}). \tag{8}$$

The heat flux q_j in Eq. (3) is given by Fourier's law for heat conduction,

$$q_j=\frac{-\mu(T)}{(\gamma-1)RePrM^2}\frac{\partial T}{\partial x_j}. \tag{9}$$

In the above equations, Re is the Reynolds number while the Prandtl number $Pr=0.72$, the ratio of specific heats $\gamma=1.4$ for air.

In the conservation laws of momentum and energy, Eqs. (2) and (3), respectively, sub-grid scale terms τ_{ij} and q_j^{sgs} are the unresolved terms and need to be modelled. In the widely used eddy-viscosity models, τ_{ij} and q_j^{sgs} are often modelled as follow:

$$\bar{\rho}\tau_{ij}=-\bar{\rho}\nu_{sgs}S_{ij}\left(\tilde{\boldsymbol{u}}\right)+\frac{1}{3}\bar{\rho}\tau_{kk}\delta_{ij}, \tag{10}$$

$$q_j^{sgs}=-\frac{\bar{\rho}\nu_{sgs}}{(\gamma-1)Pr_tM^2}\frac{\partial T}{\partial x_j}, \tag{11}$$

where ν_{sgs} is sub-grid viscosity, $Pr_t=1$ is turbulent Prandtl number (Hu *et al*., 2003).

2.2 Sub-Grid Scale Models

In the Smagorinsky model (SM),

$$\nu_{sgs}=\left(C_1\Delta\right)^2\left|S\left(\tilde{\boldsymbol{u}}\right)\right| \tag{12}$$

where the model coefficient C_1 depends on the particular flow and several values have been proposed; here $C_1=0.17$ is selected according to Schumann (1991) 's suggestion. The characteristic length scale is commonly chosen to be $\Delta=\left(\Delta_x\Delta_y\Delta_z\right)^{1/3}$, Where Δ_x, Δ_y and Δ_z are mesh sizes in the *x*, *y* and *z* directions, respectively.

It is noticeable that the SM is originally proposed for incompressible flows, where the isotropic part τ_{kk} is not modeled, but considered by modifying the pressure which appears in the momentum equation only. For compressible flows, the pressure appears in the equations of momentum, energy and the state simultaneously. Modifying the pressure to account the contributions of τ_{kk} in all these equations is undesirable. As a remedy, Vreman

(1995) suggested modelling τ_{kk} explicitly as follows:

$$\tau_{kk} = 4(C_1\Delta)^2 \left|S(\tilde{\boldsymbol{u}})\right|^2 . \tag{13}$$

The characteristic length scale of the SM depends on grid scales only, and the model coefficient C_1 is constant. The model is quite simple and easy to implement in CFD codes. But it is also known to be too dissipative, especially in predicting transitional flows.

The excessive dissipation of the SM can be overcome if the model constant is replaced by a coefficient depending on both grid scales and small scales of turbulence. The SMSM (Lenormand, *et al*., 2000) is a model of such kind. Its eddy-viscosity is given by:

$$\nu_{sgs} = C_2 |S|^{\alpha} \left(q_c^2\right)^{(1-\alpha/2)} \Delta^{(1+\alpha)} \tag{14}$$

where $\alpha = 0.5$ and $C_2 = 0.06$ is deduced from a isotropic turbulence. q_c^2 is the kinetic energy of the small scales representing the multi-scales of turbulence and is evaluated as follows:

$$q_c^2 = \frac{1}{2}\tilde{u}_i'\tilde{u}_i' \tag{15}$$

where $\tilde{u}_i'$ is fluctuating velocity extracted from the resolved velocity field: $\tilde{u}_i' = \tilde{u}_i - \hat{\tilde{u}}_i$, the caret denotes a test filter, $\hat{\tilde{u}}_i = \tilde{u}_{i-1}/4 + \tilde{u}_i/2 + \tilde{u}_{i+1}/4$, which can be interpreted as a second-order approximation of either a Gaussian filter or a top-hat filter. More explanation of evaluating q_c^2 was given by Lenormand *et al.* (2000).

In the same way of filtering the velocity, one can obtain filtered vorticity vector $\tilde{\boldsymbol{\omega}}$ from resolved vorticity vector $\tilde{\boldsymbol{\omega}}$. In order to improve the prediction of intermittent phenomena, a selective function based on the local angular θ between the vorticity vectors $\tilde{\boldsymbol{\omega}}$ and $\tilde{\boldsymbol{\omega}}$ is proposed. The θ represents local fluctuation of the flow. The flow is turbulent when the local angular fluctuation is greater than a given threshold angle θ_0. And the selective function is then given as following (Lenormand *et al*., 2000):

$$f_{\theta_0}(\theta) = \begin{cases} 1 & if \quad \theta \geq \theta_0 \\ \left[\tan(\theta/2)/\tan(\theta_0/2)\right]^4 & otherwise \end{cases} \tag{16}$$

where the value of θ_0 corresponding to the observed peak of the density probability function for the angular variation of an isotropic homogeneous turbulence (Lenormand *et al*., 2000), $\theta_0 = 20^{\circ}$. $\theta \geq \theta_0$ means the directions of two vorticity vectors change dramatically so flow is fully turbulent. While for $\theta < \theta_0$, it indicates the flow is weakly turbulent, and the eddy-viscosity decrease with θ, until the molecular viscosity is recovered at $\theta = 0$ when the flow is laminar. Based on the formulations in above, the final eddy-viscosity of the SMSM in Eq. (14) is further modified and calculated as:

$$\nu_{sgs}^{(s)} = \nu_{sgs} f_{\theta_0}(\theta) . \tag{17}$$

Another way to ease the excessive dissipation of the SM is to replace the constant eddy-viscosity coefficient, C_1, with an adjustable number C, according to the local flow dissipation. Considering the relationship between the coherent-structure and the energy dissipation, a new local sub-grid scale model was proposed by Kobayashi (2005). Such model is the aforementioned coherent-structure Smagorinsky model (CSM), in which the eddy-viscosity is given by:

$$\nu_{sgs} = C\Delta^2 \left|S(\tilde{u})\right| \tag{18}$$

where $C = C_3 \left|F_{CS}\right|^{3/2}$. The constant $C_3 = 0.05$, which is the optimized value from a priori test in a homogeneous isotropic turbulence (Kobayashi, 2005). F_{CS} is the coherent structure function defined as the second invariant of a velocity gradient tensor Q normalized by the magnitude of a velocity gradient tensor E, namely, $F_{CS} = Q/E$, where

$$Q = \frac{1}{2}\left(\frac{\partial \tilde{u}_i}{\partial x_i}\right)^2 - \frac{1}{2}\left(\frac{\partial \tilde{u}_j}{\partial x_i}\frac{\partial \tilde{u}_i}{\partial x_j}\right), \quad \text{and}$$

$$E = \frac{1}{2}\left(\frac{\partial \tilde{u}_i}{\partial x_j}\right)^2 .$$

As mentioned by Kobayashi (2005), Q is related to the energy dissipation of turbulence. The 3/2 power of F_{CS} is according to the fact $C \propto y^3$ with $Q \propto y^2$ and $E \propto \text{const}$ for incompressible flows (y is the normal direction in a wall-bounded flow). With the eddy-viscosity in Eq. (18), CSM is a closure for the sub-grid stresses.

With the idea of adjusting eddy-viscosity by the coherent-structure function, and using sub-grid scale kinetic energy as the velocity scale, Kobayashi (2005) also proposed a kinetic-energy model which was abbreviated as CKM above. The eddy-viscosity is calculated as:

$$\nu_{sgs} = C\Delta\sqrt{k_{sgs}} \tag{19}$$

where $C = C_4 \left|F_{CS}\right|$. F_{CS} is the coherent-structure function defined in the CSM. C_4 is found to be 0.15. k_{sgs} is the sub-grid scale kinetic energy, which can be calculated in a simple way, $k_{sgs} = \left(\tilde{u}_i - \tilde{u}_i\right)^2$, where the test-filtered velocity component is estimated using the Simpson rule, $\tilde{u}_i = \left(\tilde{u}_{i-1} + 4\tilde{u}_i + \tilde{u}_{i+1}\right)/6$. More details of the CSM

and CKM are provided by Kobayashi (2005).

2.3 Discretization and Solution Approach

Finite difference method (FDM) is employed for discretization of the governing equations. For the convenience of description, Eqs. (1) to (3) are rewritten in vectors as follows:

$$\frac{\partial \boldsymbol{Q}}{\partial t}=-\frac{\partial \boldsymbol{F}}{\partial x}-\frac{\partial \boldsymbol{G}}{\partial y}-\frac{\partial \boldsymbol{H}}{\partial z}+\frac{\partial \boldsymbol{F}^{v}}{\partial x}+\frac{\partial \boldsymbol{G}^{v}}{\partial y}+\frac{\partial \boldsymbol{H}^{v}}{\partial z}, \quad (20)$$

where $\boldsymbol{Q}=\left(\bar{\rho},\bar{\rho}\tilde{u},\bar{\rho}\tilde{v},\bar{\rho}\tilde{w},E_T\right)^T$, while $\boldsymbol{F}$, $\boldsymbol{G}$, and $\boldsymbol{H}$ are convection terms in *x*-, *y*-, and *z*- directions of the Cartesian coordinates system, respectively. $\boldsymbol{F}^{v}$, $\boldsymbol{G}^{v}$, and $\boldsymbol{H}^{v}$ are the viscous terms which can be easily deduced from Eqs. (1) to (3), and the superscripts '-' and '~' are omitted for simplicity of description.

Equation (20) is discretized using compatible spatial difference operators for interior points and boundary nodes. For interior points, the five-point fourth-order central schemes in the follows are employed for the first and second derivatives, respectively,

$$\begin{cases}\phi_i'=\dfrac{-\phi_{i+2}+8\phi_{i+1}-8\phi_{i-1}+\phi_{i-2}}{12\Delta h}\\ \phi_i''=\dfrac{-\phi_{i+2}+16\phi_{i+1}-30\phi_i+16\phi_{i-1}-\phi_{i-2}}{12(\Delta h)^2}\end{cases}, \quad (21)$$

where ϕ is a general function, Δh is grid-space. In the present paper, Jacobian transformation is applied to Eq. (20) so that uniform grids can be used in the transformed coordinates system. For boundary points, spatial discretization is treated using a stable high-order method based on the summation by parts (SBP) (Carpenter *et al.*, 1999). The overall spatial accuracy is fourth-order. For temporal discretization, the very low storage third-order explicit Runge-Kutta algorithm (Spalart *et al.*, 1991) is employed. This time-advancement scheme use two storage locations for three marching sub-steps,

$$\begin{cases}\boldsymbol{Q}^{n+1}=\boldsymbol{Q}^{n}+\Delta t\left(a_{21}k_1+a_{22}k_2+a_{23}k_3\right)\\ k_1=RHS\left(t_n,\boldsymbol{Q}^{n}\right)\\ k_2=RHS\left(t_n+a_{11}\Delta t,\boldsymbol{Q}^{n}+a_{11}\Delta t k_1\right)\\ k_3=RHS\left(t_n+a_{21}\Delta t+a_{12}\Delta t,\boldsymbol{Q}^{n}+a_{21}\Delta t k_1+a_{12}\Delta t k_2\right)\end{cases}, \quad (22)$$

where

$$\left(a_{11},a_{12}\right)=\left(\frac{2}{3},\frac{5}{12}\right),\quad \left(a_{21},a_{22},a_{23}\right)=\left(\frac{1}{4},\frac{3}{20},\frac{3}{5}\right),$$

RHS denotes the right hand side terms of Eq. (20), the superscripts n and n+1 are the time levels.

In order to stabilize the solution, an entropy - splitting approach (Sandham *et al.*, 2002) is employed, in which the inviscid flux is separated into conservative and non-conservative parts. The code used was previously designed for simulating shock/boundary-layer interactions (SBLI) (Sandham *et al.*, 2003), and the numerical method has been widely validated in the simulations of a variety of compressible flows (Hu *et al.*, 2003; Lai and Luo, 2007; Tullio *et al.*, 2010). General good computational efficiency and high fidelity of the numerical method have been shown in these simulations. In the present study, the code parallelized using the message-passing-interface (MPI) protocol is rewritten and changed into parallelized using the OpenMP method so that it can also be run on the memory-shared multi-core workstations.

3. PREPARATIONS OF THE SIMULATION

3.1 The Parallel Jet

The compressible parallel jet studied by Hu *et al.* (2003) is selected as the testing case for the present comparison of SGS models. The jet is at a Mach 0.9 and a Reynolds number of 2000, based on the jet velocity U_j and the jet slot width D_j. Namely, $\mathrm{Re}_j=D_j\rho_\infty U_j/\mu_\infty=2000$, $M_j=U_j/c_\infty=0.9$, where ρ_∞, μ_∞, c_∞ are the referential values of density, dynamic viscosity and sound speed in the far field, respectively.

The computational domain is shown in Fig. 1. The dimensionless size (normalized by D_j) in the streamwise, lateral and spanwise directions (depicted as *x*-, *y*-, and *z*-) are $L_x=24$, $L_y=15$, and $L_z=3$, respectively. The grid points in the *x*-, *y*- and *z*- are 181×181×16, with the stretched mesh in the *x*-*y* plane shown in Fig. 1. The grid nodes in the *z*-direction are uniformly spaced. For grid sensitivity check, another mesh with 181×181×32 grid nodes is also employed for LES.

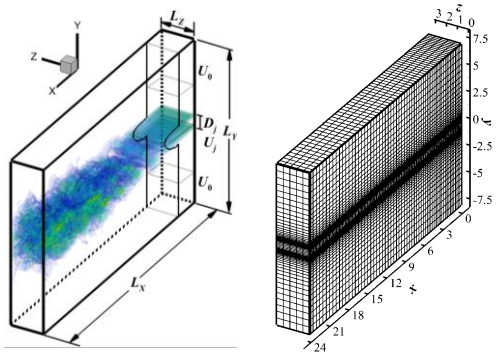

(a) Computational domain (b) The Mesh

Fig. 1. Computational domain and the Mesh (One in every three lines is shown in each direction).

For convenience of calculating the statistics, the simulations are marching in time with a fixed dimensionless time step of $\Delta t=0.003075\left(D_j/U_j\right)$,

which can satisfy *CFL* < 1 on both meshes.

The initial shear thickness is known to have a considerable influence on the development of the jet. As shown in Fig. 1, the computational domain starts from the parallel nozzle exit, so a laminar streamwise velocity profile is imposed according to Hu *et al*. (2003) 's suggestion as follows:

$$\begin{cases} u = \frac{1}{2}\left(U_j - U_{co}\right)\left(\tanh\left(\left(y + D_j/2\right)/h\right)\right. \\ \quad \left. - \tanh\left(\left(y + D_j/2\right)/h\right)\right) + U_{co} + u_p \\ v = v_p \\ u_p = 0.33y^2\left(4y^2 - 1\right)e^{-6y^2}\sin\left(2\pi z/L_z\right)\cos\left(2t\right) \\ v_p = 0.4y^3 e^{-6y^2}\sin\left(2\pi z/L_z\right)\sin\left(2t\right) \end{cases}, \quad (23)$$

where two hyperbolic tangent profiles are used and the shear thickness is set to $h = 0.1D_j$. Clearly, the inflow velocity profile is a top-hat with a co-flow velocity of $U_{co} = 0.1U_j$, with a three-dimensional disturbance applied to the streamwise and cross-flow velocities (u_p, v_p) at a single frequency and a single spanwise wavenumber. The parameters in Eqs. (23) are carefully chosen based on linear instability analysis so as to trigger the symmetric mode of the parallel jet and minimize the spurious inflow waves which may generate. These inflow perturbations are shown to be sufficient for trigger the turbulence (Hu *et al*., 2003). In addition to the inflow velocity, the temperature is initialized according to Crocco-Busemann temperature-velocity relationship, written as:

$$T = 1 + 0.5(\gamma - 1)M_j^2\left(1 - u^2\right). \quad (24)$$

Except the velocity and the temperature profiles, the pressure at the inflow boundary is assumed to be uniform and equals to the referential background pressure; these result in the inflow conditions as follows:

$$p = 1/\left(\gamma M_j^2\right), \ \rho = 1/T \ . \quad (25)$$

With all these inflow conditions, the flow field is initialized. The non-reflection conditions introduced by Thompson (1987) are used to allow all outgoing waves propagate smoothly out of the computational domain and to minimize the numerical reflection. Concisely, the outgoing characteristics are explicitly calculated and allowed to move out of the domain from the bounds in the *x*- and *y*- directions. In the spanwise direction (z-), periodic boundary conditions are applied as generally done for three dimensional spatially evolving jet flows.

3.2 Tests of the Settings

As mentioned in above, the algorithm has been validated over a variety of problems, so only two issues are checked in the present calculation. These are the specified spanwise length L_z and the grid sensitivity of the LES results.

The periodic conditions applied at spanwise boundaries are a compromise to simulating the parallel jet, because of the computational cost. The larger spanwise length L_z for the computational domain is used, the closer approach to the parallel jet can be achieved. However, the mesh for mapping the computational domain increases linearly with L_z. In order to save computational resource, the periodic conditions in the spanwise boundaries are employed as a remedy, subjecting to the fact that the spanwise size needs to be large enough to avoid non-physical flow interference in this direction. In order to check the spanwise size of the computational domain, the correlation of velocity components in spanwise direction is defined as follows:

$$R_{u_i u_i}(\Delta z) = \frac{\left\langle u_i'(z_0)u_i'(z_0 + \Delta z)\right\rangle}{\sqrt{\left\langle u_i'^2(z_0)\right\rangle}\sqrt{\left\langle u_i'^2(z_0 + \Delta z)\right\rangle}} \quad (26)$$

where u_i' represents a fluctuating velocity component, $\langle\bullet\rangle$ denotes the time-averaged, z_0 is the *z*- location of spanwise boundary while Δz is the space gap from z_0. Temporal range of averaging is *t* = 72~240 corresponding to 3 ~ 10 flow-through of the computational domain, and the sampling interval is the marching step Δt. There are 54640 samples in total for the averaging.

Figure 2 shows the correlations of velocity components at a monitoring point (*x*,*y*,z_0)=(16,-1,0). It can be observed that the correlation lines decay to approximately zero within half of the specific spanwise length L_z, indicating the spanwise size of the computational domain is large enough while possible non-physical flow interference in this direction is successfully cancelled.

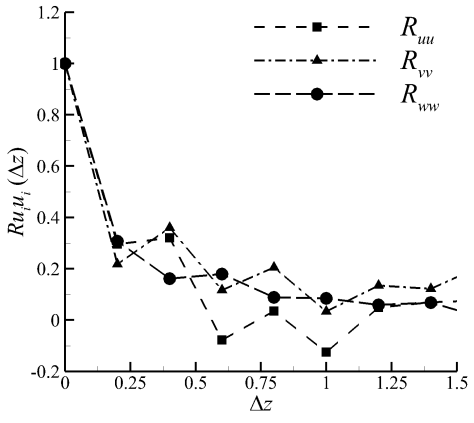

Fig. 2. Spanwise correlation of velocity components between (16,-1,0) to (16,-1,1.5).

The resolution quality is an important issue for LES. For a practical way to measure the resolution quality is to make use of the resolved turbulent kinetic energy k^{res} on a grid and the extrapolated

total turbulent kinetic energy k^{tot} based on two grids (Pope, 2004). The index of LES resolution quality is a ratio of these turbulent kinetic energy, $LES\_IQ = k^{res}/k^{tot}$, as proposed by Celik *et al.* (2005). The procedure is briefed as following:

As only a part of the turbulent kinetic energy in the physical flow can be resolved by LES, Celik *et al.* (2005) suggested that the difference between k^{tot} and k^{res}, termed as the effective sub-grid scale kinetic energy and denoted as k^{eff_sgs}, can be approximated by:

$$k^{tot} - k^{res} = k^{eff\_sgs} = a_k \Delta^p , \tag{27}$$

where the superscript p is the order of accuracy of the numerical scheme, a_k is a coefficient to be determined. To determine the a_k, Eq. (27) is supposed to be applicable to the same flow depicted by both a coarser mesh and a finer one, then we have:

$$\begin{cases} k^{tot} - k_c^{res} = a_k \Delta_c^p \\ k^{tot} - k_f^{res} = a_k \Delta_f^p \end{cases}, \tag{28}$$

where subscripts 'c' and 'f' denote quantities obtained on the coarser and finer meshes, respectively. Because k_c^{res} and k_f^{res} are results from LES, the equation group (28) can be solved to find k^{tot} and a_k. Then we can have:

$$a_k = \left[\left(k_f^{res} - k_c^{res}\right)/\left(\beta^p - 1\right)\right]/\Delta_f^p ,$$

where $\beta = \Delta_c/\Delta_f > 1$ is the grid-size ratio. Celik *et al.* (2005) then gave the quality indices of LES for fine and coarse grids, denoted by LES_IQ_f and LES_IQ_c respectively, as:

$$LES\_IQ_f = 1\Big/\left[1 + \left|1 - k_c^{res}/k_f^{res}\right|/\left(\beta^p - 1\right)\right], \tag{29}$$

$$LES\_IQ_c = 1\Big/\left[1 + \left|k_f^{res}/k_c^{res} - 1\right|\beta^p/\left(\beta^p - 1\right)\right]. \tag{30}$$

In order to carry out this check, the aforementioned two meshes of 181×181×16 and 181×181×32 are considered. The dimensionless time range for finding the Reynolds averaged variables k_c^{res} and k_f^{res}, is t = 48 ~ 72, with 7804 samples. Fig. 3 shows the turbulent kinetic energy along lip-line, calculated with CSM on two meshes. The turbulent kinetic energy is weak at the beginning of the jet, and then increases rapidly to reach a peak. After that, the curves fall down along the streamwise direction. The curves obtained using the two meshes have a similar shape, and the coarse-grid result is slightly higher than that of the fine-grid. The calculated quality index is shown in Fig. 4. LES_IQ_c is approximately 75% while LES_IQ_f is about 85% in the most range of the spanwise locations in the jet, both of which are fairly good for an acceptable LES. Considering the computational cost, the coarser mesh is used in the followed simulations.

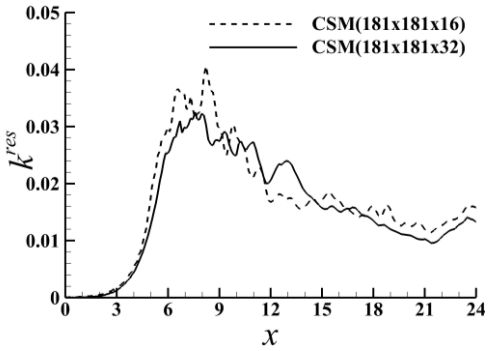

Fig. 3. The turbulent kinetic energy along lip-line resolved with CSM on coarse-grid shown in dashed line and fine-grid shown in solid line.

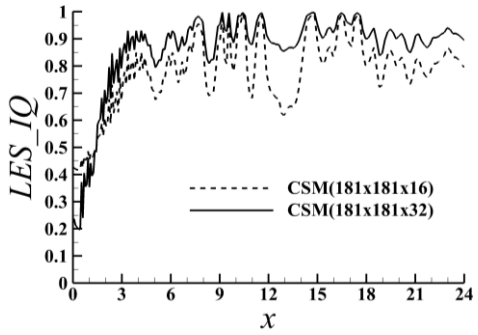

Fig. 4. Large eddy simulation index of quality (*LES_IQ*) along the lip-line for coarser-grid shown in dashed line and fine-grid shown in solid line.

4. RESULTS AND DISCUSSIONS

4.1 Averaged Flow-Field

The profiles of the averaged streamwise velocity $\langle u \rangle$ obtained with the four SGS models are presented and compared in Fig. 5. The experimental data of Bradbury (1965), Gutmark (1976) and Rampaprian (1985) are also shown. Similarity coordinates are used, with the abscissa axis normalized by the local jet half-width $\delta_{0.5}$ (explain later), while the vertical ordinate is normalized by the difference of centerline velocity and co-flow velocity, ΔU_c. The self-similarity appears in the turbulence region where the flow reaches equilibrium between the generated turbulent kinetic energy from the main flow and the dissipated energy by viscosity at the small scales (Hussein *et al.*, 1994). Consequently, all the flat hat profiles at the inflow develop in the streamwise direction, and the normalized velocity profiles at various streamwise locations finally collapse to one curve till x > 8. The comparison shows the results from large eddy simulation using the four SGS models are in good agreement with the experiments data,

indicating that all the four models are capable of predicting the averaged streamwise velocity.

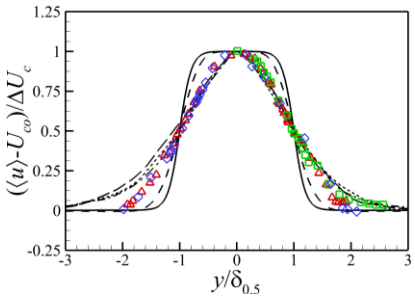

(a) SM.

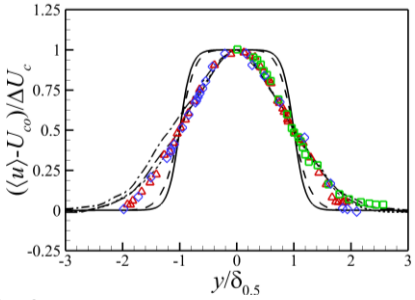

(b) SMSM.

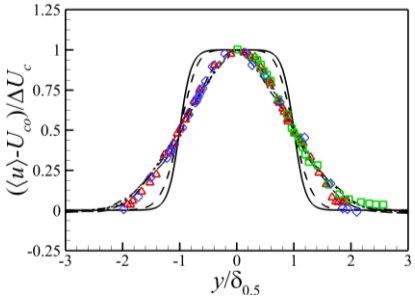

(c) CSM.

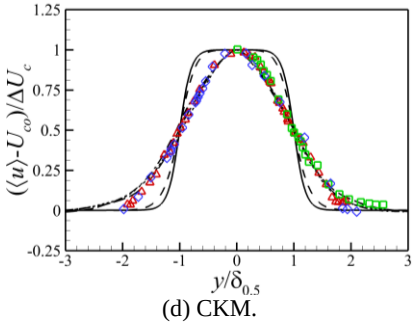

(d) CKM.

x = 0; *x* = 4; *x* = 8; *x* = 20; *x* = 22; Bradbury (1965); Gutmark (1976); Ramaprian (1985)

Fig. 5. The averaged velocity profiles at different streamwise locations.

The power spectra density E_f of the streamwise velocity fluctuations at five streamwise locations along the lip-line are shown in Fig. 6 for SM. The instantaneous velocity signals are sampled in the time range of t = 48~216, with 54640 samples. Figure 6 shows the E_f at x = 2 is relatively weak. From x = 2 to x = 6, the energy scales in E_f are increased, corresponding to the development of Kelvin- Helmholtz instabilities. Between x = 8~20, the spectra exhibits an energy cascade which is quite similar to the -5/3 slope for fully developed turbulence. In addition, the inertial stage is observed in these spectra, indicating the grid is capable of resolving the wide range of scales in the energy cascade.

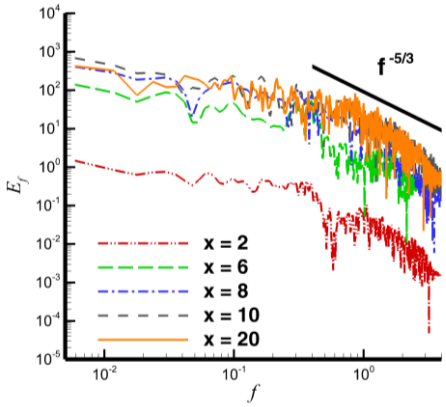

Fig. 6. Dimensionless power spectra of the velocity signals along the jet lip line at five locations for SM.

The normalized jet centerline streamwise velocity U_c (normalized by U_j), averaged from time t = 72~240, is shown in Fig. 7. Basically the U_c predicted by these four models keeps equal to 1 in the beginning of the jet, representing the potential core in this range. Then U_c starts to decrease at the end of the potential core. The distance from the nozzle exit to the point where $U_c = 0.99$ is often mentioned as the length of the potential core. Seeing from Fig. 7, the predicted length of the potential is 6.93, 6.35, 5.84 and 5.8, for the SM, CSM, SMSM and CKM,, respectively. The longest potential core length predicted by the SM means the latest flow transition. In downstream of the potential core, U_c decreases gradually. Experiments and analysis results on plane jets have shown that U_c deceases at a -1/2 power, $U_c = 1.2/\sqrt{0.724 \cdot x/D_j}$ (Tollmien, 1926). The results in Fig. 7 show that the SMSM, the CSM and the CKM model have well predicted the decrease of U_c, while the profile predicted by the SM decreases faster than the experimental equation.

Flow mixing is significant within the shear layer. To discuss the development of shear layer, the half-width or the center of shear layer of the jet, $\delta_{0.5}$, defined as the lateral position where $u(\delta_{0.5}) = 0.5(U_c + U_{co})$, is shown in Fig. 8(a). The result shows that $\delta_{0.5}$ has a two-staged growth, i.e., the early stage of slower linear growth in the potential-core region and the stage of faster linear growth immediately after the potential core. The four SGS models predict a similar growth rate, but

the SM gives a higher value at the downstream. The vorticity thickness of shear layer is defined as $\delta_\omega = |U_c - U_{co}| \Big/ \left|\left(\overline{\partial u/\partial y}\right)_{max}\right|$ (Sandhu and Sandham 1994); its results of the present jet are shown in Fig. 8(b). Comparison shows that the SM predicts the smallest thickness within most of x region, while the other three localized models give a similar result. Considering that the averaged velocity profiles are well predicted and have good agreements between the four SGS models, the velocity difference between the both sides of the shear-layer maybe regarded as constant when different SGS models are employed. Therefore, the thicker shear-layer thickness means the stronger flow mixing and weaker gradient of velocity across the shear-layer. The result of thinner shear-layer in the result of the SM model, on the other hand, indicates a stronger gradient of velocity in the lateral direction, which needs generally a higher viscosity to smooth it. Such results may be explained by the well known excessive dissipation of the SM.

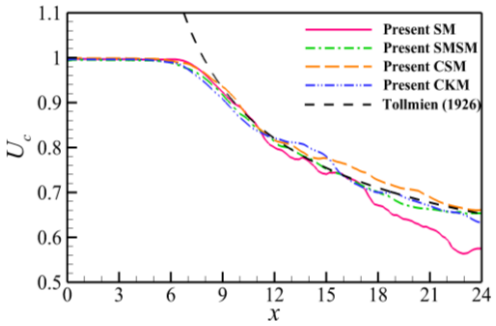

Fig. 7. The averaged jet centerline velocity U_c.

4.2 Instantaneous Flow

The contours of instantaneous vorticity magnitude snapped at t = 82 are shown in Fig. 9, where the DNS result of Hu *et al.* (2003) at the same time is also included for comparison. The potential core, paring of vortices, formation of large vortical structures and their fragmentation into smaller sized eddies during the flow transition are observable. The extent of lateral developments predicted by the SM, the SMSM, the CSM and the CKM are shown in Fig. 9(b ~ e), respectively. It can be seen that, the result of the SM has the smallest lateral development. The CKM has a wider lateral size of the vortical distribution than the SM. For the SMSM and the CSM, their predicted distributions of vortices in the lateral range are comparable to the DNS results. The resolved vortical scales in the result of SM are quite limited. The CKM gives a relatively better result than the SM, but the resolved scales are still not rich. For the SMSM and the CSM, again, their resolved vortical scales are quite similar. In an early paper of the authors (Liu *et al.*, 2018), the SMSM was compared with the DSM, it was shown the DSM obtained a worse agreement with the DNS results, seeing from the scales resolved in the vortical structures, so further comparison with the DSM is not included in this paper. As pointed by Lai and Luo (2007), the over-predicted turbulent viscosity by the SM may have lowered down the effective Reynolds number of the flow, which smears the small vortical scales.

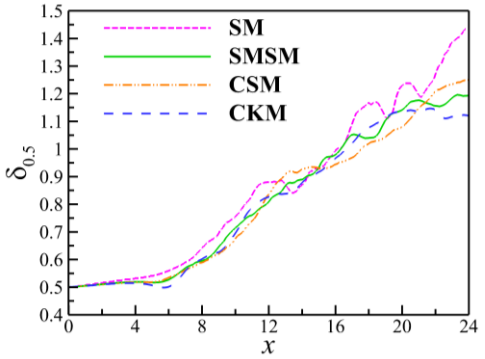

(a) Evolution of $\delta_{0.5}$ along jet centerline.

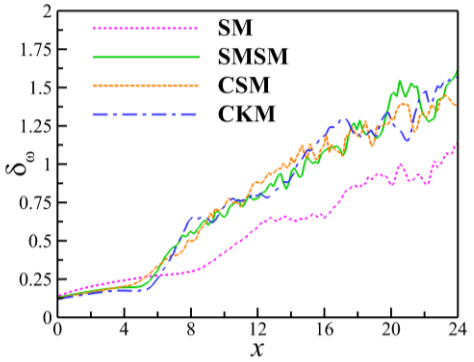

(b) Evolution of δ_ω along jet centerline.

Fig. 8. Comparison of the predicted shear layer developments.

The three-dimensional distribution of turbulence eddies represented by the Q- criterion is shown in Fig. 10, where the shown instantaneous iso-surface is Q=0.1 and is snapped at time t = 207 without losing generality for a qualitative comparison. The positive Q value means the rotation of flow is in domination and strain is relatively weak, thus the location of a vortex is separated from shearing flow (Jeong, 1995). For the SM and the CKM, shown in Figs. 10(a) and (d), respectively, some small-scale longitudinal vortices are observable even near the outflow boundary where the flow is assumed to be fully developed. It means that both the SM and the CKM are too dissipative, so the small-scale eddies are expected to disappear quickly and large ones are remained. While for the SMSM and the CSM, the fully developed turbulence with plenty of small - scale eddies are shown in Figs.10 (b) and (c), respectively. More turbulent small scale eddies are resolved in the results of SMSM and the CSM, as compared with those of the SM and the CKM.

Development of small scale eddies can be influenced by viscosity. The instantaneous contour of the sub-grid dynamic viscosity $\mu_{sgs} = \rho \nu_{sgs}$ is shown in Fig. 11. It can be seen that μ_{sgs} predicted

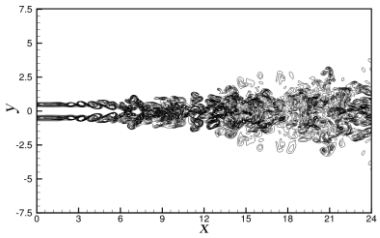

(a) DNS, in Hu *et al*. (2003).

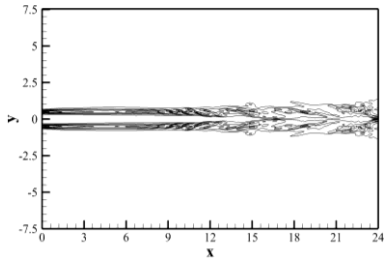

(b) Present LES using SM.

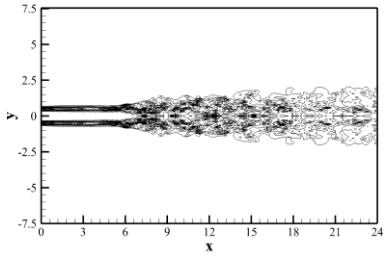

(c) Present LES using SMSM.

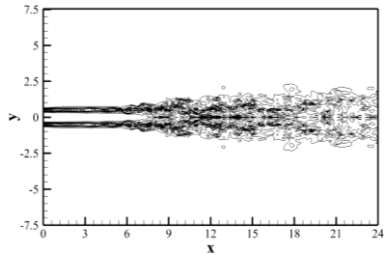

(d) Present LES using CSM.

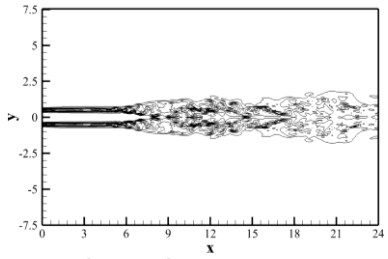

(e) Present LES using CKM.

Fig. 9. Comparison of instantaneous vorticity magnitudes on mid-span plane at t = 82. 9 Contour levels are shown in the range of 0.5~5.

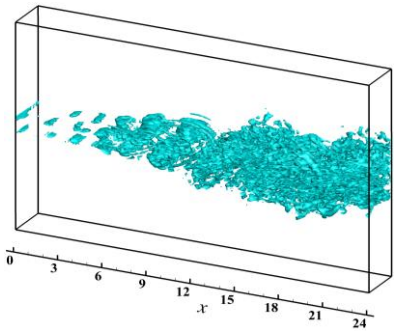

(a) SM.

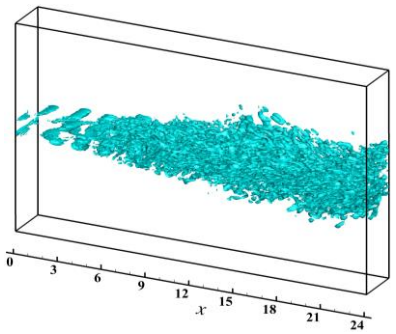

(b) SMSM.

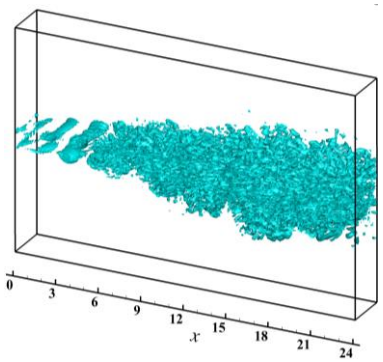

(c) CSM.

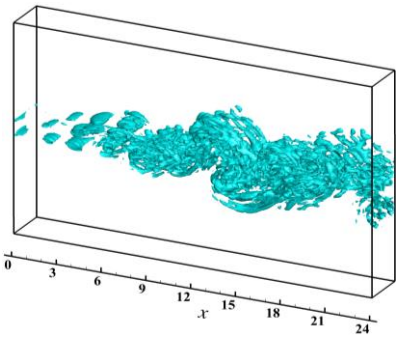

(d) CKM.

Fig. 10. Comparison of iso-surface of Q = 0.1 in the present LES, at t = 207.

by the SM has noticeable value even in the potential core region (in Fig. 11(a)), and is like two long parallel ribbons from the inflow boundary to the flow transition zone. In Fig. 11(d), μ_{sgs} predicted by the CKM has spurious values even in the inflow boundary, which indicates the SGS viscosity is over-predicted. These over-predicted μ_{sgs} may lead to the exceed dissipation of small scale eddies, which is consistent with the results in Figs. 9(b) and (e). The μ_{sgs} predicted by both the SMSM and the CSM are nearly zero value within the potential core. Only till the end of potential core where flow

transition starts, the value of μ_{sgs} rises up gradually and forms a laterally expending distribution, as shown in Figs. 11(b) and (c).

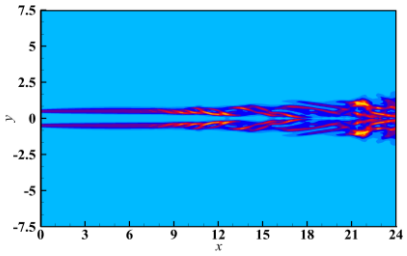

(a) SM.

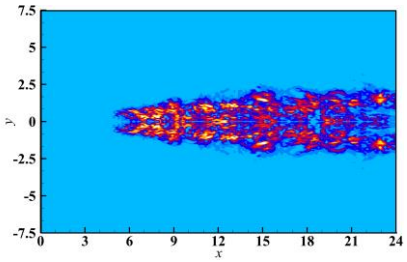

(b) SMSM.

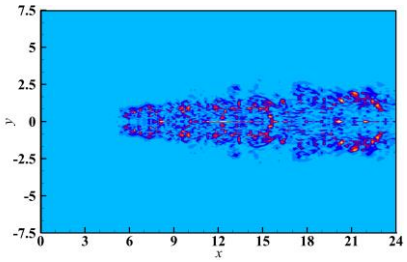

(c) CSM.

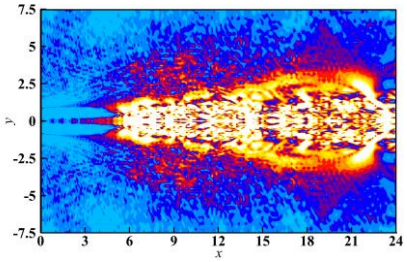

(d) CKM.

Fig. 11. Distributions of μ_{sgs} on mid-span plane at t = 82 for four SGS models.

The instantaneous molecular dissipation $\varepsilon_{\mu} = \mu S_{ij}\left(\partial u_i/\partial x_j\right)$ (Vreman, 1995) is compared in Fig. 12, where the distributions at t = 82 are shown. It can be seen that within the potential core, where the flow is supposed to be laminar, the distributions of ε_{μ} predicted by these models all appear in a shape of two parallel ribbons, their length in the streamwise direction vary, as discussed in Fig. 7. The instantaneous sub-grid-scale dissipation $\varepsilon_{sgs} = \rho\tau_{ij}\left(\partial u_i/\partial x_j\right)$ at t = 82 as well, and also refer to Vreman (1995) for the definition, is shown in Fig. 13. Comparison between Figs. 12 and 13 reveals that the distributions of ε_{sgs} and ε_{μ} predicted by the SM are quite similar, and their contour values are of the same order. But on the contrary, the ε_{sgs} in Figs. 13(b) to (d) and predicted by the SMSM, CSM, and CKM respectively, have values of nearly zero within the potential core. Such differences in the predicted ε_{sgs} indicate that the SM cannot predict the change of effective viscosity during transition, while the methods of locally adjusting model coefficients work well when the flow regimes is changed between the laminar and turbulent states.

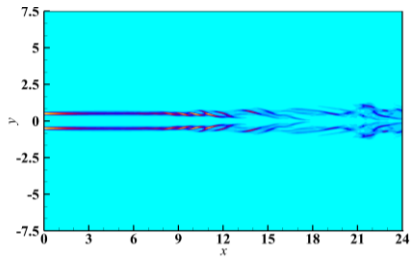

(a) SM.

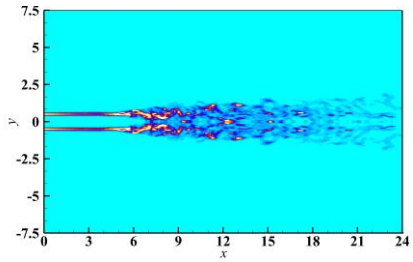

(b) SMSM.

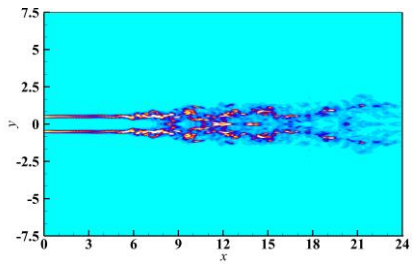

(c) CSM.

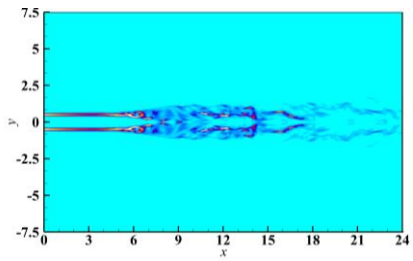

(d) CKM.

Fig. 12. Contours of ε_{μ} on mid-span plane at t = 82 predicted by four SGS models.

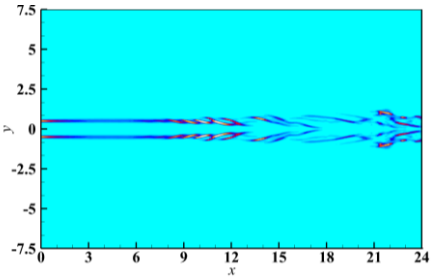

(a) SM

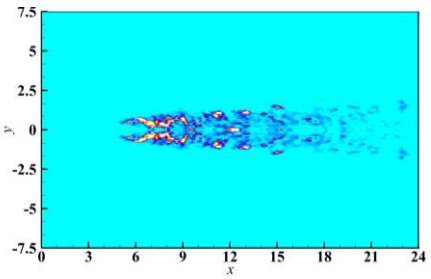

(b) SMSM

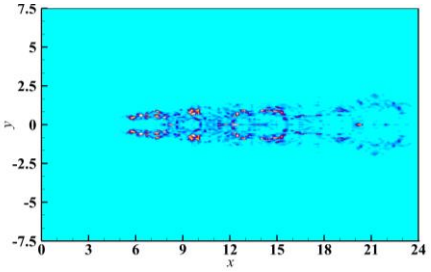

(c) CSM

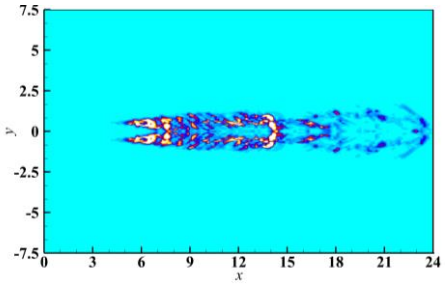

(d) CKM

Fig. 13. Contours of ε_{sgs} on mid-span plane at t = 82 predicted using four SGS models.

Figures 14 are contours of the θ and $f_{\theta_0}(\theta)$. It can be seen that in the potential core, the θ is nearly zero while the corresponding $f_{\theta_0}(\theta)$ obtained from Eq. (16) is also almost zero. As aforementioned, θ is the angular between two vorticity vectors on grid scale and test grid scale respectively, the zero values of θ indicate the laminar flow region. The selective function $f_{\theta_0}(\theta)$ reflects flow transition correctly; its distribution is consistent with the predicted μ_{sgs} in Fig. 11(b) and the ε_{sgs} in Fig. 13(b).

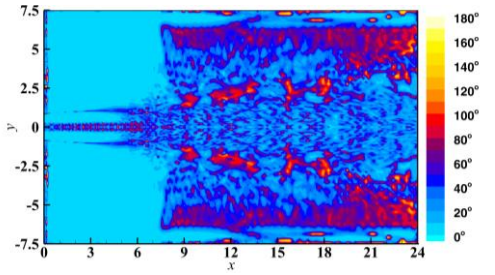

(a) θ

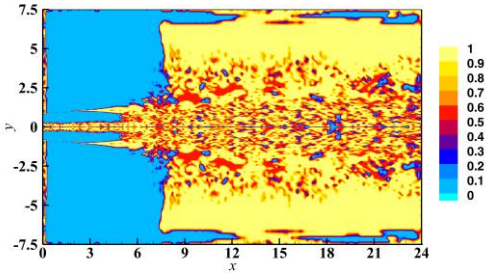

(b) f_{θ_0}

Fig. 14. Contours of θ and f_{θ_0} in mid-span plane at t = 82.

4.3 Turbulence Statistics

The statistics of fluctuating velocity products, $\langle u'u' \rangle$, in the mid-span plane are shown in Fig. 15. In the potential core, the flow is laminar while values of the statistic are zero. At the end of potential core, turbulent fluctuations set on, representing the transition of flow. As shown in Fig. 15, the peak value of $\langle u'u' \rangle$ might be as high as above 0.03. The high fluctuation regions appear just at the end of the potential core, and set to weakening along the streamwise direction with the development of the jet, as predicted by the SMSM and the CSM and shown in Figs. 15(b) and (c), respectively. In the result of the SM, shown in Fig. 15(a), the fluctuation strength weakens along the jet as well, but the weakening is at a slower rate. This slower weakening rate is consistent with the longitudinal vortices predicted by the SM in Fig. 10(a), which appear in a wide streamwise range from the potential core to almost the outflow bound of the computational domain. Such longitudinal vortices are of moderate size which can cause strong fluctuations. For the result of $\langle u'u' \rangle$ predicted by the CKM and shown in Fig. 15(d), however, the fluctuation strength is relatively weaker than those predicted by the other three models. Such result is not surprising if the vortical structures in Fig. 10 are considered. As shown in Fig. 10(d), the vortices predicted by the CKM are clearly less than those of the counterparts in Fig. 10. Especially, although longitudinal vortices also appear in a wide streamwise range in Fig. 10(d), the small scale vortices in the map are clearly less than those predicted by the SMSM and CSM, and even clearly less than the results of SM. The weaker vortical flow in the result of CKM is

reasonable and consistent with its lower fluctuations.

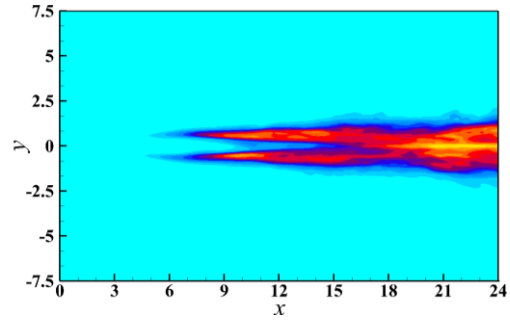

(a) SM.

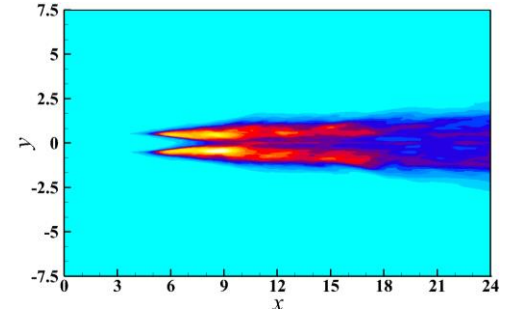

(b) SMSM.

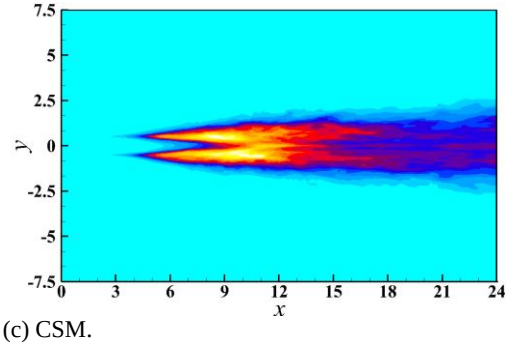

(c) CSM.

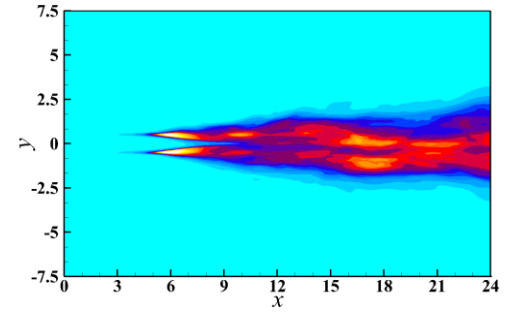

(d) CKM.

Fig. 15. Predicted distributions of $\langle u'u' \rangle$ in the mid-span plane using four SGS models.

4.4 Balances of Momentum Equation

In order to evaluate the contributions of fluctuation to the transport of momentum, and to compare the predictions of these four SGS models, the balance of the momentum equation is considered. The Favre's mass weighted filtered momentum Eq. (2) can be further averaged in time and in the *z*-direction, which results:

$$\underbrace{\frac{\partial \langle \bar{\rho} \rangle \langle \tilde{u}_i \rangle \langle \tilde{u}_j \rangle}{\partial x_j}}_{1} + \underbrace{\frac{\partial \langle \bar{p} \rangle}{\partial x_i}}_{2} - \underbrace{\frac{\partial \langle \sigma_{ji} \rangle}{\partial x_j}}_{3} + \underbrace{\frac{\partial \langle \bar{\rho} u_i'' u_j'' \rangle}{\partial x_j}}_{4} = - \underbrace{\frac{\partial \langle \bar{\rho} \tau_{ji} \rangle}{\partial x_j}}_{5} \tag{31}$$

where all the variables are resolved on the grid scale, and $\langle \bullet \rangle$ denotes the time-averaged variables. As the jet is statistically stable, the temporal derivative disappears in the averaged Eq. (31). For convective term, mass-weighted velocity is considered, so $\langle \bar{\rho} \tilde{u}_i'' \rangle = 0$, and the resolved turbulent stress is $\langle \bar{\rho} \tilde{u}_i'' \tilde{u}_j'' \rangle = \langle \bar{\rho} \tilde{u}_i \tilde{u}_j \rangle - \langle \bar{\rho} \rangle \langle \tilde{u}_i \rangle \langle \tilde{u}_j \rangle$. The other terms are obtained only by averaging in time. The time range for averaging is t = 48~216 corresponding to 2~9 flow-through times of the computational domain, with an interval of sampling equal to 100 marching steps ($100 \Delta t$). Totally, 540 instantaneous results are sampled for averaging. Then the averaged 3D flow-field is further averaged in the *z*-direction to obtain the picture in the *x*-*y* plane. While the terms 1~5 represent mean convection, the pressure gradient, the molecular viscous stress, the resolved turbulent stress, and the sub-grid stress, respectively. In these terms, the resolved turbulent stress $\langle \bar{\rho} u_i'' u_j'' \rangle$ associates with the product of resolved fluctuating velocity, while the sub-grid stress $\langle \bar{\rho} \tau_{ji} \rangle$ is the modeled part of the sub-grid scale fluctuations. In Eq. (31), terms with i = 1, j for dummy index give a balance of the mean streamwise momentum, $\langle \bar{\rho} \rangle \langle \tilde{u}_1 \rangle$. Figure 16 shows the balance at x = 8. The dominant balance is between the mean convection and the gradient of the resolved turbulent stress $\partial \langle \bar{\rho} u_1'' u_j'' \rangle / \partial x_j$ (Le Ribault, 1999). All the four models predict a peak value of the mean convection, and the resolved turbulent stress term with an opposite peak at the same lateral location is shown. The peak values of the localized models are similar; however, their values are nearly three times higher than that of the SM. Therefore, the convection and turbulent fluctuations predicted by the localized models are stronger than those predicted by the SM. In the meantime, the lower peak values of the mean convection and turbulent fluctuations in the results of SM mean that the SGS stress term has contributed more percentages in the total balance, as compared with the other three models. As a result, the flow predicted by the SM is more dependent on the model itself than the other models.

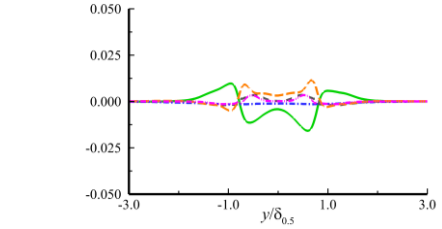

(a) SM.

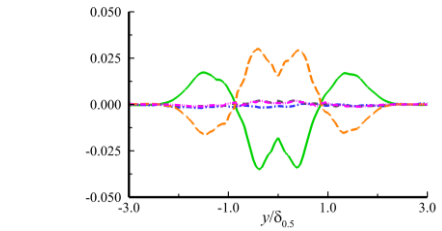

(b) SMSM.

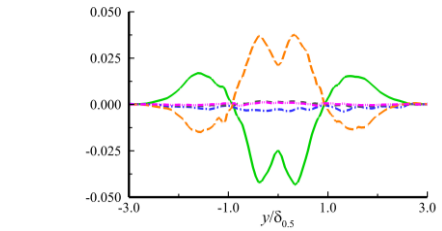

(c) CSM.

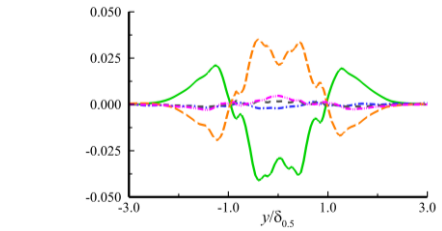

(d) CKM.

term (1); term (2); term (3); term (4); term (5)

Fig. 16. Balance of the streamwise momentum equation at x = 8. (terms in Eq. (31), i = 1 and j is dummy index).

The distribution of sub-grid stress term in streamwise $-\partial\langle\bar{\rho}\tau_{j1}\rangle/\partial x_j$ is shown in Fig. 17. This term, modeled by the SGS model, represents the averaged momentum on the sub-grid scale. $-\partial\langle\bar{\rho}\tau_{j1}\rangle/\partial x_j$ behaves as the source term for the averaged transport equation of momentum. A negative value of $-\partial\langle\bar{\rho}\tau_{j1}\rangle/\partial x_j$ means removing momentum from resolved flow, while a positive value means adding momentum to the resolved flow. It can be seen that the SM predicts strong sub-grid stresses along the shear layer within the potential core region and gives negative values from the beginning of the jet. This is consistent with its defect of lowering down the effective Reynolds number. In addition, the CKM also gives excessive negative values around the transition region and positive values along the centerline in the downstream. Such strong momentum exchanges between the resolved grid-scale and unresolved sub-grid scale in the transition region may explain the good prediction of fluctuations by the CKM, although the μ_{sgs} is already over-predicted as shown in Fig. 11(d).

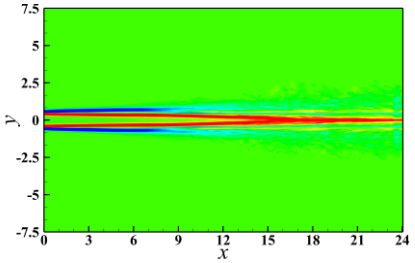

(a) SM.

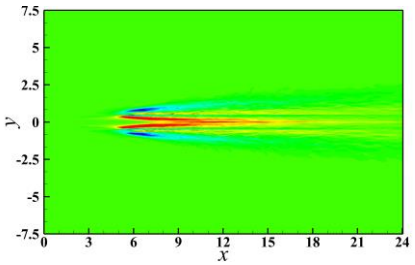

(b) SMSM.

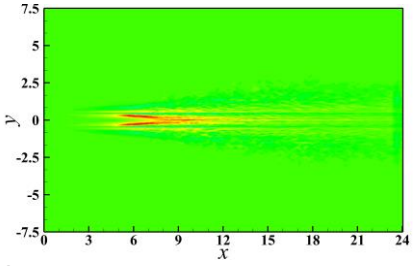

(c) CSM.

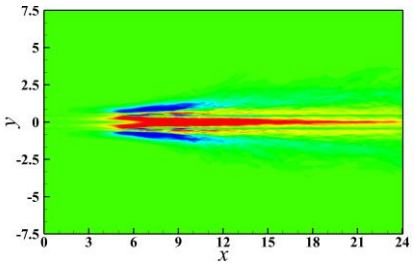

(d) CKM.

Fig. 17. Distribution of the SGS stress term $-\partial\langle\bar{\rho}\tau_{j1}\rangle/\partial x_j$ in the mid-span plane.

Finally, the computational efficiency of the four models is compared by showing the CPU time records in Table 1. Slight differences between these four models exist. Ratio of CPU time respect to the SM for SMSM, CKM and CSM is 1.3, 1.2 and CSM=1, respectively.

Table 1 CPU time per grid point per time step

SGS model	SM	SMSM	CSM	CKM
CPU time μs	1064	1371	1065	1300

5. CONCLUSIONS

Large eddy simulations of a three dimensional parallel jet at a Reynolds number 2000 and Mach number 0.9 have been carried out. The computational domain size and the grid sensitivity of the LES are checked. Four SGS models the SM, the SMSM, the CSM and the CKM are compared. Both the predicted averaged and instantaneous flow-fields are analyzed and carefully compared. The main conclusions are summarized as follows:

1. The SMSM and the CSM are capable of predicting the multi-scaled vortical structures in the turbulent jet, while the CKM and the SM over-predict the SGS viscosity and dissipation in the potential core flow region. The CKM and SM have smeared small scale vortical motions by lowering down the effective Reynolds number of the jet. Such defect is more serious for the SM.

2. Examinations of the mean momentum balances show that the SMSM, the CSM and the CKM are capable to resolve the strong mean convection and the turbulent energy during the flow transition. It may partially explain that the CKM gives similar averaged results as the other localized models though the instantaneous dissipation is over-predicted by the CKM. The SM over-predicted the percentage of the SGS energy in the total balance, so the flow is more dependent on the model itself.

3. The SMSM and the CSM have performed well in predicting both the averaged and the instantaneous flow-fields of the compressible jet. The two localized models which are computationally efficient and easy for coding are recommended for the LES of the compressible jet.

ACKNOWLEDGEMENTS

Authors are grateful to the National Natural Science Foundation of China (NSFC) for funding this research under Grants 51576067 and 91852111. Special thanks are given to Professor N. D. Sandham and Dr Z. Hu from the University of Southampton in the UK for their permission and assistance in using the SBLI code.

REFERENCES

Bodony, D. J. and S. K. Lele (2008). Current status of jet noise predictions using large-eddy simulation. AIAA Journal 46(2), 364-380.

Bradbury, L.J.S. (1965). The structure of a self-preserving turbulent plane jet. Journal of Fluid Mechanics 23 Part1, 31-64.

Carpenter, M. H., J. Nordstrom, and D. Gottlieb (1999). A stable and conservative interface treatment of arbitrary spatial accuracy. Journal of Computational Physics 148, 341-365.

Celik, I. B., Z. N. Cehreli and I. Yavuz (2005). Index of resolution quality for large eddy simulations. Journal of Fluids Engineering 127, 949-958.

Everitt, K.W. and A. G. Robins (1978). The development and structure of turbulent plane jets. Journal of Fluid Mechanics 88 Part3, 563-583.

Gutmark, E. and I. Wygnanski (1976). The planar turbulent jet. Journal of Fluid Mechanics 73, 465-495

Hu, Z. W., C. L. Morfey and N. D. Sandham (2003). Large eddy simulation of plane jet sound radiation. AIAA 2003-3166: 1-8.

Hui, H., T. Kobayashi, S. Wu, and G. Shen (1999). Changes to the vortical and turbulent structure of jet flows due to mechanical tabs. Proceedings of the Institution of Mechanical Engineer 213 Part C, 321-329.

Hussein, J. P. Steven and K. William (1994). Velocity measurements in a high Reynolds number, momentum-conserving, axisymmetric, turbulent jet. Journal of Fluid Mechanics 258, 31-75.

Jeong, J. and F. Hussain (1995). On the identification of a vortex. Journal of Fluid Mechanics 285, 69-94.

Klein, M., A. Sadiki and J. Janicka (2003). Investigation of the influence of the Reynolds number on a plane jet using direct numerical simulation. International Journal of Heat and Fluid Flow 24, 785-794.

Kobayashi, H. (2005). The subgrid-scale models based on coherent structures for rotating homogeneous turbulence and turbulent channel flow. Physics of Fluids 17, 045104.

Lai, H. and K. H. Luo (2007). A three dimensional hybrid LES acoustic analogy method for predicting open cavity noise. Flow, turbulence and Combustion 79, 55-82.

Larchevêque, L., P. Sagaut, I. Mary and O. Labbe (2003). Large-eddy simulation of a compressible flow past a deep cavity. Physics of Fluids 15, 193-210.

Le Ribault, C., S. Sarkar and S. A. Stanley (1999). Large eddy simulation of a plane jet. Physics of Fluids 11, 3069.

Lenormand, E., P. Sagaut, L. T. Phuoc and P. Comte (2000). Subgrid-scale models for large-eddy simulations of compressible wall bounded flows. AIAA Journal 38, 1340-1350.

Lighthill, M. J. (1952). On sound generated aero-dynamically. I. general theory. Proceedings of the Royal Society A: Mathematical, Physical and Engineering Sciences 211, 564-587.

Liu, Q., C. He, and H. Lai (2018). Large eddy simulation of a plane jet and comparison of SGS models. Journal of Engineering Thermo-physics 39, 1272-1278.

Mary, I. and P. Sagaut (2002). Large eddy simulation of fluid around an airfoil near stall. AIAA Journal 40, 1139-1145.

Piomelli, U. (1999). Large-eddy simulation: achievements and challenges. Progress in Aerospace Sciences 35, 335-362.

Pope, S. B. (2004). Ten questions concerning the large-eddy simulation of turbulent flows. New Journal of Physics 6(35)

Ramaprian, B. R. and M. S. Chandrasekhara (1985). LDA measurements in plane turbulent jets. Transactions of the ASME 107, 264-271.

Sagaut, P. (2007). Implicit large eddy simulation. In Grinstein, F. F., Margolin, L. G. and Rider, W. J. (Eds.), Subgrid-Scale Modeling: Issues and Approach¬es, Cambridge University Press.

Sandham, N. D., C. L. Morfey and Z. W. Hu (2006). Non-linear mechanisms of sound generation in a perturbed parallel jet flow. Journal of Fluid Mechanics 565, 1-23.

Sandham, N. D., Q. Li and H. C. Yee (2002). Entropy splitting for high-order numerical simulation of compressible turbulence. Journal of Computational Physics 178, 307-322

Sandham, N. D., Y. F. Yao and A. A. Lawal (2003). Large-eddy simulation of transonic turbulent flow over a bump. International Journal of Heat and Fluid Flow 24, 584-595.

Sandhu, H. S. and N. D. Sandham (1994). Boundary conditions for spatially growing compressible shear layers. QMW-EP-1000

Schumann, U. (1991). Direct and large eddy simulation of turbulence - summary of the state-of-the-art. Lecture Series 1991-02: Introduction to the modeling of turbulence, Von Karman Institute, Brussels.

Spalart, P. R., R. D. Moser and M. M. Rogers (1991). Spectral methods for the Navier-Stokes equations with one infinite and two periodic directions. Journal of computational physics 96, 297-324.

Stanley, S. A., S. Sarkar and P. J. Mellado (2002). A study of the flow-field evolution and mixing in a planar turbulent jet using direct numerical simulation. Journal of Fluid Mechanics 450, 377-407.

Tam, C. K. W. (1998). Jet noise: since 1952. Theoretical and computational fluid dynamics 10, 393-405.

Tam, K. W. and L. Auriault (1999). Jet mixing noise from fine-scale turbulence. AIAA Journal 37, 145-153.

Tanahashi, M., T. Miyauchi and K. Matsuoka (1997). Coherent fine scale structures in temporally developing mixing layers. In K. Hanjalic and T. W. J. Peeters (Eds.), Turbulence, Heat and Mass Transfer 2, Proceedings of Second International Symposium on Turbulence, Heat and Mass Transfer, Dekft Ubiversity Press, Delft, the Netherlands, 461-470.

Thompson, K W. (1987). Time dependent boundary conditions for hyperbolic systems, II. Journal of Computational Physics 68, 1-24.

Tinney, C. E. and P. Jordan (2008). The near pressure field of co-axial sub-sonic jets. Journal of Fluid Mechanics 611, 175-204.

Tollmien, W. (1926). Berechnung turbulenter Ausbreitungsvorgänge. ZAMM - Journal of Applied Mathematics and Mechanics 6(6), 468-478.

Tullio, N. D. and N. D. Sandham (2010). Direct numerical simulation of breakdown to turbulence in a Mach 6 boundary layer over a porous surface. Physics of Fluids 22, 1-15.

Uzun, A. and M. Y. Hussaini (2012). Some issues in large-eddy simulations for chevron nozzle jet flows. Journal of Propulsion and Power 20(2), 246-258.

Vreman B. (1995). Direct and Large Eddy Simulation of the Compressible Turbulent Mixing Layer.Ph. D. thesis, the Netherlands: University of Tewnte.

Wan, Z. H., L. Zhou, H. H. Yang and D. J. Sun (2013). Large eddy simulation of flow development and noise generation of free and swirling jets. Phys¬ics of fluids 25, 1-27.